ARTICLE

Check for updates

Iron isotopes constrain sub-seafloor hydrothermal processes at the Trans-Atlantic Geotraverse (TAG) active sulfide mound

Fredrik Sahlström [1,2✉], Valentin R. Troll [3], Sabina Strmić Palinkaš[1,4], Ellen Kooijman[5] & Xin-Yuan Zheng [6]

Sub-seafloor hydrothermal processes along volcanically active plate boundaries are integral to the formation of seafloor massive sulfide deposits and to oceanic iron cycling, yet the nature of their relationship is poorly understood. Here we apply iron isotope analysis to sulfide minerals from the Trans-Atlantic Geotraverse (TAG) mound and underlying stockwork, 26°N Mid-Atlantic Ridge, to trace hydrothermal processes inside an actively-forming sulfide deposit in a sediment-free mid-ocean ridge setting. We show that data for recently formed chalcopyrite imply hydrothermal fluid–mound interactions cause small negative shifts (<-0.1‰) to the δ^{56}Fe signature of dissolved iron released from TAG into the North Atlantic Ocean. Texturally distinct types of pyrite, in turn, preserve a δ^{56}Fe range from -1.27 to $+0.56$‰ that reflects contrasting precipitation mechanisms (hydrothermal fluid–seawater mixing vs. conductive cooling) and variable degrees of progressive hydrothermal maturation during the >20 kyr evolution of the TAG complex. The identified processes may explain iron isotope variations found in fossil onshore sulfide deposits.

[1] Department of Geosciences, UiT The Arctic University of Norway, 9037 Tromsø, Norway. [2] Geological Engineering Program, Pontificia Universidad Católica del Perú, San Miguel 15088, Lima, Peru. [3] Department of Earth Sciences, Uppsala University, 752 36 Uppsala, Sweden. [4] Centre for Deep Sea Research, Department of Earth Science, University of Bergen, 5007 Bergen, Norway. [5] Department of Geosciences, Swedish Museum of Natural History, 114 18 Stockholm, Sweden. [6] Department of Earth and Environmental Sciences, University of Minnesota – Twin Cities, Minneapolis, MN 55455, USA. ✉email: fredrik.sahlstrom@uit.no

Seafloor massive sulfide (SMS) deposits form as part of submarine hydrothermal systems that are driven by volcanism along both divergent and convergent plate boundaries[1–3]. They are a potential future source of metals deemed critical for technology and industry (e.g., copper, zinc, and gold)[4] and represent modern analogs to volcanogenic massive sulfide (VMS) deposits currently exploited in ancient volcanic successions onshore[5]. In addition, hydrothermal venting atop active SMS deposits creates a unique biological habitat that is argued to have supported early life on Earth[6,7] and fluxes a wide range of chemicals from the oceanic crust into the oceans. In this context, it is increasingly recognized that hydrothermal vents are contributors to the oceanic inventory of dissolved iron, a key micronutrient that regulates phytoplankton growth and hence the biological carbon pump[8–13].

SMS genesis is considered to involve (1) exhalative sulfide deposition, forming chimney and mound structures and vent-distal stratiform ores at the seafloor, and (2) sub-seafloor infilling and replacement of primary hydrothermal precipitates and underlying volcanic material by sulfide[5,14–18]. Sub-seafloor mineralization in particular is shown to be key in producing large-tonnage sulfide deposits, yet the nature of the different hydrothermal processes involved remains poorly constrained[5,15,16,18]. Since evidence for such processes is commonly obscured by geologic overprinting in fossil onshore VMS deposits, ocean drilling of active SMS systems represents a crucial source of information for detailed characterization of sub-seafloor hydrothermal activity in a range of tectonic settings[18–22]. To this end, stable iron isotopes in sulfides from the internal portions of an active SMS deposit offer a method to further elucidate sub-seafloor hydrothermal processes, including their role in the oceanic (bio-)geochemical cycling of iron[23]. Moreover, such in situ sub-seafloor iron isotope data have the potential to better resolve existing iron isotope interpretations for hydrothermal vents and plumes atop active SMS systems and can help reconcile them with observations from fossil onshore VMS deposits and from experimental studies of high-temperature hydrothermal sulfide formation[8,13,24–34], which would broaden the applicability of iron isotopes as a geochemical tracer.

Here, we apply iron isotope analysis of sulfide minerals to a suite of historical drill cores from the Trans-Atlantic Geotraverse (TAG) active mound and stockwork complex of the north-central Mid-Atlantic Ridge (Fig. 1). The TAG complex formed through intermittent cycles of high-temperature hydrothermal activity over at least the last 20,000 years[35–37] and its detailed growth history includes repeated hydrothermal precipitation at and below the mound surface, mechanical and hydrothermal reworking of earlier formed precipitates, and progressive alteration and partial incorporation of the basaltic host rocks[15,19,38,39]. Building on this geologic and hydrothermal framework, we use our new sulfide iron isotope data to further constrain sub-seafloor hydrothermal processes at TAG and assess their implications for ore formation and for iron cycling in the North Atlantic Ocean. The unique insights gathered from our study of TAG will likely enhance the utility of iron isotopes to the investigation of active and fossil seafloor hydrothermal systems elsewhere.

The TAG mound and stockwork complex. The TAG active sulfide mound was discovered in 1985[40] at the E margin of the rift valley of the slow-spreading Mid-Atlantic Ridge at 26°N (Fig. 1) and is located in an area featuring several inactive sulfide and oxide deposits[41–43]. Following its discovery, TAG was the first-ever SMS deposit investigated by the Ocean Drilling Program (ODP) in 1994[44,45] and it is now one of the World's most comprehensively characterized modern seafloor hydrothermal systems. The mound is located about 2.5 km E of the neovolcanic zone of the ridge at

~3670 m water depth. It forms a distinctly circular structure composed of two superposed terraces, and it measures ~200 m in basal diameter and rises ~50 m above the seafloor[19,46] (Fig. 1b). The mound is underlain by a ~80 m diameter, pipe-shaped stockwork of mineralized and intensely altered basaltic basement rocks that extends to at least 125 m below the surface[19,38] (Fig. 2a). The mound and underlying stockwork are estimated to contain a combined mass of ~3.9 million tonnes of sulfide with an average grade of 1–2% copper. The morphology, size, and bulk composition of TAG is comparable to that of some VMS deposits preserved in ophiolites, e.g., those exploited in Cyprus, in Oman, and in Newfoundland[47].

Presently, high-temperature (360–370 °C), copper-rich black smokers are discharged from a cluster of chalcopyrite-pyrite-anhydrite chimneys situated on top of a ~20 m diameter cone structure in the NW part of the upper terrace (the 'Black Smoker Complex'; Figs. 1b and 2a)[48–50]. A field of sphalerite-dominated, beehive-shaped chimneys occurs on the lower terrace ~70 m SE of the Black Smoker Complex and is named the 'Kremlin Area' (Figs. 1b and 2a). Prior to and during ODP drilling, these chimneys vented white smokers that were distinctly colder (260–300 °C) and were copper-iron-poor, but zinc-rich relative to the black smoker discharges. These white smokers were suggested to have evolved from an end-member hydrothermal fluid via conductive cooling and mixing with entrained seawater, and precipitation of sulfides and anhydrite, within the mound[48–50]. The white smoker venting was, however, observed to have ceased during revisits in 2003 and later[51].

The mound surface is made up entirely of hydrothermal precipitates including plate-like crusts and bulbous blocks of porous massive sulfide as well as siliceous iron oxyhydroxide sediments[15]. Oxidized pyrite-rich sulfide talus and debris flows form an apron that surrounds and partially covers the steep-sided margins of the mound[48]. Below the surface, the upper part of the mound (0 to ~15 m.b.s.f.) consists of massive pyrite and massive pyrite breccias with locally abundant iron oxyhydroxides, chert, chalcopyrite, sphalerite, and marcasite[15,19,39,44,52] (Fig. 2a). The massive pyrite zone is underlain by an anhydrite-rich zone made up of pyrite-anhydrite and pyrite-silica(-anhydrite) breccias that extends down to ~45 m.b.s.f. (Fig. 2a). The breccias in this zone are extensively crosscut by up to ~45 cm thick, composite anhydrite veins with localized sulfide mineralization[53]. The pyrite-silica(-anhydrite) breccias at the base of the anhydrite-rich zone define the transition from the mound to the upper part of the stockwork, which comprises pyrite-silica breccias that grade into silicified wallrock breccias with depth[39] (Fig. 2a). Below ~100 m.b.s.f., the silicified wallrock breccias eventually transition into chloritized basalt breccias that are overprinted by multiple generations of pyrite, quartz, and quartz-pyrite stringer veins[19] (Fig. 2a).

Results

Iron isotope compositions were determined for a total of 50 micro-drilled sulfide separates encompassing the main rock types from the vertical and lateral extent of the TAG mound and the underlying stockwork (Fig. 2a). The TAG sulfides show an overall range of $\delta^{56}Fe$ values between -1.27 and $+0.56‰$, with a mean value of $+0.04‰$ ($\pm0.08‰$ 2σ; Table 1, Supplementary Data 1). Notably, variations in $\delta^{56}Fe$ values are observed between the different textural types of sulfide analyzed, including (following ref. [53]): (1) massive sulfide; (2) vein-related sulfide; (3) sulfide in clasts from different breccia types; and (4) disseminated sulfide in altered basalt host rock.

Massive sulfide. Massive sulfide (sulfide-only) samples from the upper portions of the TAG mound are dominated by fine-grained, variably porous pyrite that in places preserves primary colloform and spheroidal textures[15] (Fig. 2b). Similar variably
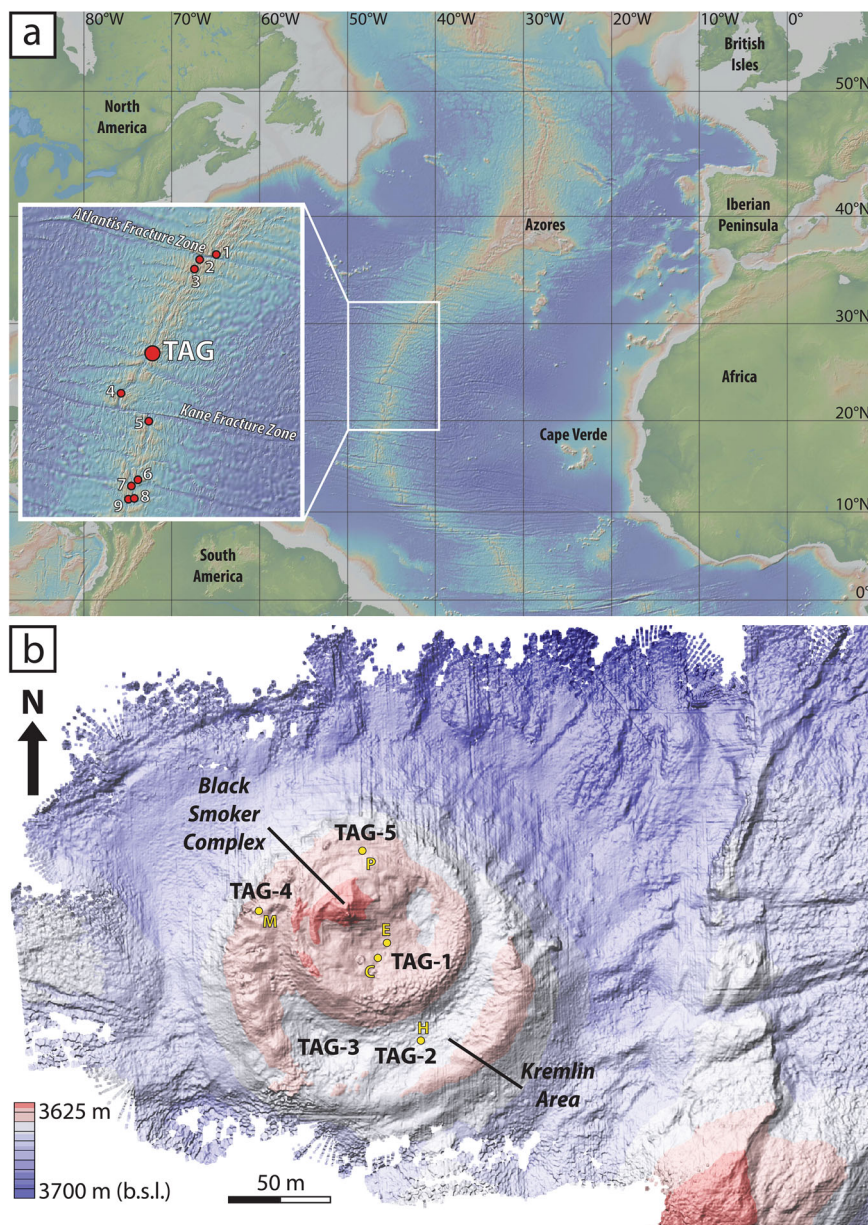
Fig. 1 Bathymetric maps with sampling locations. a Location of TAG and other hydrothermal vent fields and sulfide deposits (red symbols) along the TAG segment, north-central Mid-Atlantic Ridge: 1—Lost City; 2—MAR 30°N; 3—Broken Spur; 4—MAR 24°30′N; 5—Snakepit; 6—Surprise; 7—Puy des Folles; 8—Zenith-Victory; 9—Yubileinoe. Map modified from ref. [68] and ref. [69] and retrieved via GeoMapApp (http://www.geomapapp.org). **b** Detailed map of the TAG mound showing the collar locations of the ODP Leg 158 drill cores used in this study (957C, 957E, 957H, 957M, and 957P). Map modified from ref. [70] and retrieved via GeoMapApp.

porous massive sulfide occurs locally also as cement in silicified wallrock breccias at deeper levels. Pyrite from massive sulfide samples shows a mean $\delta^{56}Fe$ value of −0.42‰ and a range from −1.27 to +0.28‰ ($n = 9$; Table 1, Supplementary Data 1).

Vein-related sulfide. The anhydrite vein networks within the pyrite-anhydrite and pyrite-silica(-anhydrite) zones contain sulfides locally. Fine-grained pyrite and chalcopyrite are aggregated in bands or clots within the veins (Fig. 2c), with more voluminous sulfide present in selvages and halos along the vein margins[15,19,53]. Pyrite samples from the anhydrite veins and selvages show $\delta^{56}Fe$ values between −0.52 and +0.06‰ with a mean of −0.24‰ ($n = 5$), whereas co-existing chalcopyrite records $\delta^{56}Fe$ values between −0.04 and +0.08‰ with a mean of +0.01‰ ($n = 3$; Table 1, Supplementary Data 1).

Coarse-grained pyrite from quartz-pyrite stringer veins cross-cutting the chloritized basalt breccias in the deeper parts of the TAG stockwork (Fig. 2e) shows $\delta^{56}Fe$ values between +0.09 and +0.38‰ with a mean of +0.22‰ ($n = 3$; Table 1, Supplementary Data 1).

Sulfide in breccia clasts. Clasts of massive sulfide occur throughout the pyrite, pyrite-anhydrite, pyrite-silica(-anhydrite), and the pyrite-silica breccias at TAG (Fig. 2d). The breccia clasts range from a few mm up to >5 cm in diameter and are chiefly made up of compact, granular aggregates of polycrystalline euhedral pyrite[15]. Some sulfide clasts, however, contain fine-grained microporous domains that preserve remains of colloform and spheroidal mineral textures, whereas some other clasts exhibit sequential growth banding[15]. Locally preserved microcrystalline
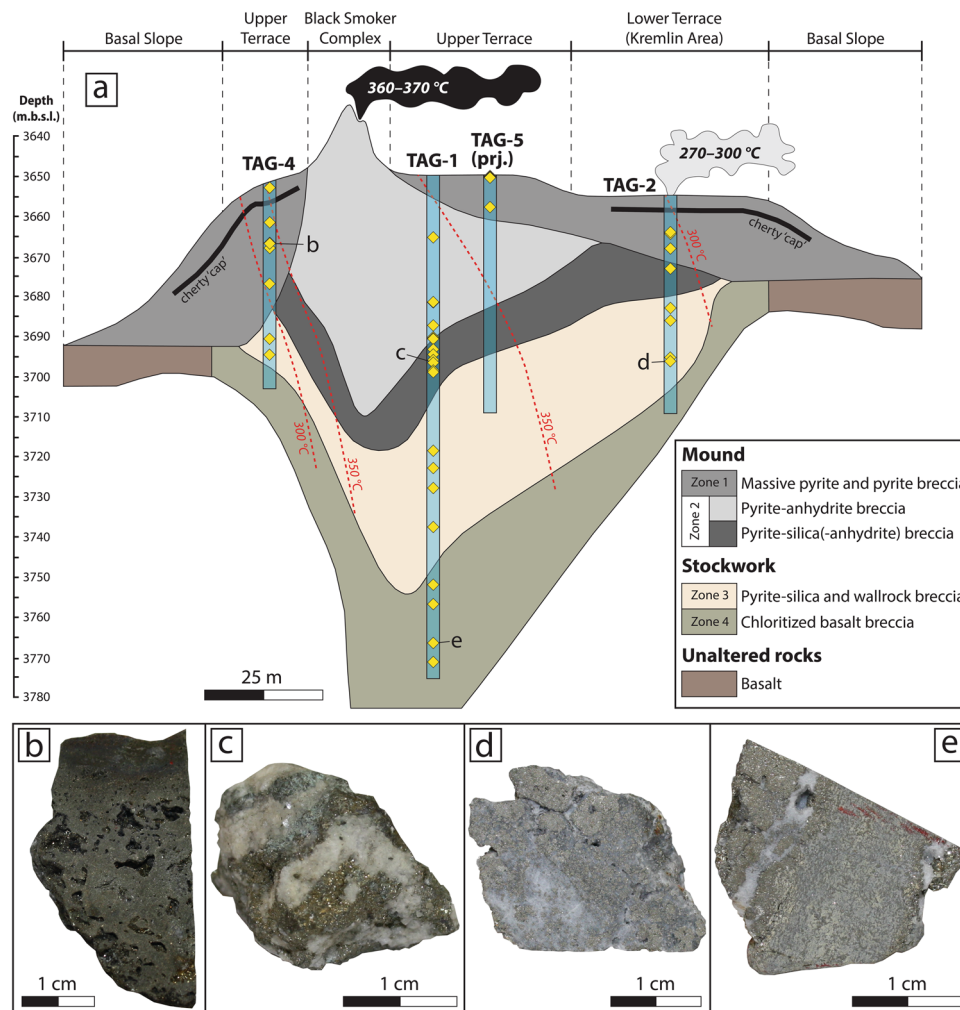
Fig. 2 Internal structure of TAG and examples of sampled sulfide textures. a Composite section through the TAG mound and underlying stockwork drawn based on multiple drill cores in each area; TAG-5 is projected onto the section. The samples utilized in this study (yellow diamonds) encompass the main rock types from the vertical and lateral extent of TAG[19,44]: massive pyrite and pyrite breccia (types 5 and 6); pyrite-anhydrite breccia (type 7) and pyrite-silica(−anhydrite) breccia (type 8), both with abundant anhydrite veins (type 11); pyrite-silica and silicified wallrock breccia (types 9 and 10a); and chloritized basalt breccia (type 10b). Vent fluid temperatures for the Black Smoker Complex and the (now inactive) Kremlin Area are from ref. [49] and isotherms are drawn based on fluid inclusion data[39,71]. Figure modified from ref. [52] and ref. [69]. **b** Massive sulfide mineralization from the upper parts of the mound comprising fine-grained and porous pyrite and marcasite with local chalcopyrite. The top part of the rock piece preserves a colloform texture (TAG-4, 957M, 14.79 m.b.s.f.). **c** Aggregates of pyrite and chalcopyrite (partly oxidized, greenish in photo) within a fragment of an anhydrite vein from the lower part of the mound (TAG-1, 957C, 46.69 m.b.s.f.). **d** Pyrite-silica breccia from the upper part of the stockwork comprising clasts of massive granular pyrite in a matrix of quartz and pyrite (TAG-2, 957H, 41.32 m.b.s.f.). **e** Fragment of chloritized basalt host rock with finely disseminated pyrite from the deeper part of the stockwork. The altered basalt is crosscut by quartz-pyrite stringer veins (TAG-1, 957E, 116.42 m.b.s.f.).

Table 1 Summary of iron isotope data for TAG sulfides.

Sample type	Mineral	n	Mean δ^{56}Fe (‰)^a	Mean 2σ	Minimum δ^{56}Fe (‰)^a	Maximum δ^{56}Fe (‰)^a
Overall	Pyrite, Chalcopyrite	50	0.04	0.08	−1.27	0.56
Massive sulfide	Pyrite	9	−0.42	0.08	−1.27	0.28
Sulfide in anhydrite veins	Pyrite	5	−0.24	0.07	−0.52	0.06
Sulfide in anhydrite veins	Chalcopyrite	3	0.01	0.07	−0.04	0.08
Sulfide in quartz-pyrite stringer veins	Pyrite	3	0.22	0.07	0.09	0.38
Sulfide in breccia clasts	Pyrite	22	0.12	0.09	−0.32	0.37
Disseminated sulfide in altered basalt host rock	Pyrite	8	0.47	0.07	0.34	0.56

^{a}δ^{56}Fe corresponds to ^{56}Fe/^{54}Fe ratio relative to IRMM-14 international standard.

pyrite textures are also noted and may represent a precursor to some coarser pyrite clasts[15]. Pyrite from the breccia clasts exhibits δ^{56}Fe values between −0.32 and +0.37‰ with a mean of +0.12‰ (n = 22; Table 1, Supplementary Data 1).

Disseminated sulfide in altered basalt host rock. The finely disseminated pyrite samples extracted from within variably altered basalt fragments in the silicified wallrock and chloritized basalt breccias of the TAG complex (Fig. 2e) yield a mean δ^{56}Fe

value of +0.47‰ and a range from +0.34 to +0.56‰ ($n = 8$; Table 1, Supplementary Data 1).

Discussion

Assessment of hydrothermal fluid iron isotope fractionation within the TAG mound. In a typical mid-ocean ridge setting, the iron content and isotopic composition of the hydrothermal fluid is initially set during high-temperature leaching and alteration of basalt in the reaction zone. This process is suggested to enrich the hydrothermal fluid in iron that is isotopically light (^{56}Fe-depleted) relative to MORB (δ^{56}Fe$_{MORB} \approx +0.1$‰)[23,25,54–56]. Upon entering and migrating through a large sulfide mound such as TAG, the fluid will be progressively modified through mineral precipitation in open spaces as well as hydrothermal reworking of pre-existing precipitates along its path to the seafloor[14,57]. However, it remains unclear in how far hydrothermal fluid iron isotope compositions are affected (fractionated) during such interaction[24–26].

Experimental studies have indicated that chalcopyrite precipitating within seafloor hydrothermal systems rapidly achieves iron isotopic equilibrium with the co-existing fluid and hence chalcopyrite δ^{56}Fe values can be used to assess hydrothermal fluid compositions[31]. Utilizing the fractionation factor provided by ref. [31] (i.e., Δ^{56}Fe$_{chalcopyrite-Fe(aq)} = 0.09 \pm 0.17$‰, 2σ), three vein-related chalcopyrite samples from the lower part of the TAG mound (30–50 m.b.s.f.) yield equilibrium fluid δ^{56}Fe values of -0.13 to -0.01‰ (± 0.18‰, 2σ; Supplementary Data 1), which are about 0.1 to 0.25‰ lower than MORB values[23,56]. The range of our inferred δ^{56}Fe$_{fluid}$ values overlaps with and extends to slightly higher values relative to recently (1998) measured vent fluids from the Black Smoker Complex (-0.17 to -0.11 ± 0.02‰, 2σ)[28]. Since anhydrite within the TAG mound dissolves during inactive periods (i.e., retrograde solubility), the preservation of anhydrite in the chalcopyrite-bearing veins indicates that they formed during the current high-temperature hydrothermal cycle that commenced at ~100 years ago[37,39,58,59]. Our inferred and the measured[28] fluid datasets can thus be interpreted in conjunction and imply that recent TAG hydrothermal fluids experience small negative shifts in their δ^{56}Fe values (<-0.1‰) during ascent through the mound to the black smoker vent site. Such limited evolution of fluid δ^{56}Fe values during upflow, in turn, suggests that the competing effects of rapid pyrite precipitation that lead to increased fluid δ^{56}Fe values versus those of hydrothermal maturation of pyrite and precipitation of chalcopyrite that decrease fluid δ^{56}Fe values (discussed further below) may largely cancel each other out. Alternatively, sub-seafloor sulfide mineralization is volumetrically minor relative to the total flux of dissolved iron through the TAG hydrothermal system. Following venting, oxidation of Fe^{2+} and precipitation of iron oxyhydroxides within the TAG hydrothermal plume are invoked to cause a more extensive decrease in the δ^{56}Fe values of dissolved iron, down to -1.35‰[13,32]. This final volume of dissolved iron with low δ^{56}Fe values has been observed to then travel in seawater via currents up to thousands of kilometers away from the TAG site, likely influencing surface planktonic activity in the North Atlantic Ocean[13].

Our results now allow us to track the isotopic evolution of dissolved iron throughout the TAG hydrothermal system and reveal an overall and stepwise decrease in δ^{56}Fe values. This finding expands our knowledge on the sequence of (bio-)geochemical processes that contribute to the iron isotopic signature of hydrothermally sourced iron[8,24–29,32,54] and will thereby help to further refine identification and quantification of such iron in the global oceans and in associated sedimentary records[8,13,60].

Evolution of sub-seafloor mineralization at TAG constrained by pyrite δ^{56}Fe values. Based on the δ^{56}Fe$_{fluid}$ values from ref. [28] and those calculated in this study, combined with the iron isotope fractionation factors of ref. [30] and ref. [34], the range of δ^{56}Fe values of pyrite in equilibrium with recent TAG hydrothermal fluids is expected to be +0.45 to +1.32‰ (including the 2σ uncertainty; Fig. 3). Notably, only a small subset of our pyrite data plot within this range (6 out of 47; Fig. 3, Supplementary Data 1). However, unlike chalcopyrite, formation of pyrite in seafloor hydrothermal systems has been proposed to occur via transient precursor mineral species that may impose kinetic effects on iron isotope fractionation[26,30,34,61,62]. On the basis of a synthesis of available experimental and theoretical data, ref. [34] proposed a two-stage model for the formation and iron isotopic equilibration of hydrothermal pyrite at high temperature (>300 °C). In this model, a rapid (few days) initial stage of pyrite formation occurs via an inferred aqueous iron (poly)sulfide precursor phase whose detailed nature (stoichiometry, coordination and magnetic spin) depends on the hydrothermal fluid composition. This inferred short-lived iron (poly)sulfide precursor obtains iron isotopic equilibrium with the fluid, and its δ^{56}Fe signature is then transferred without fractionation upon conversion to pyrite. The initial pyrite will thereby be out of iron isotopic equilibrium with the hydrothermal fluid and will have a δ^{56}Fe value that may be up to ~1.5‰ lower than the value expected for pyrite in equilibrium with the fluid (Δ^{56}Fe$_{pyrite-Fe(aq)} \approx 0.8-1$‰ at 300–450 °C)[30,34]. The δ^{56}Fe$_{pyrite}$ value will then gradually increase toward this equilibrium value during a subsequent and much slower stage of pyrite recrystallization and iron isotopic equilibration with the hydrothermal fluid[30,34].

Rates of $\gtrsim$1 year to reach pyrite–fluid iron isotopic equilibrium have been estimated under ideal (experimental) conditions[34]. However, it is not clear what timescales apply to iron isotope equilibration in pyrite in natural SMS systems and how equilibration is influenced by different precipitation mechanisms and by progressive hydrothermal maturation[26,52,63]. Here we attempt to shed further light on these aspects and integrate our texturally resolved pyrite iron isotope dataset into a refined geologic and hydrothermal framework of TAG[15,19,35–39,52].

The lowest δ^{56}Fe$_{pyrite}$ values at TAG are found in the massive sulfide mineralization concentrated in the upper parts of the mound (Fig. 3, Table 1). These values are distinctly lower than the estimated δ^{56}Fe values of pyrite in equilibrium with TAG hydrothermal fluids (Fig. 3) and they partly overlap with δ^{56}Fe$_{pyrite}$ values reported from seafloor sulfide chimneys elsewhere[25,26]. The most negative δ^{56}Fe$_{pyrite}$ values in our sample suite reach down to -1.27‰ and correspond to porous massive sulfide samples from TAG-4 that exhibit well-developed colloform textures (Fig. 2b). The preservation of such primary depositional features in the massive sulfide and its chimney-like pyrite iron isotope signature are consistent with recent formation at or near the mound surface by growth into open space[15]. Here, mixing between hydrothermal fluid and cold seawater likely led to rapid precipitation of pyrite with kinetically-driven low δ^{56}Fe values (i.e., strong pyrite–fluid disequilibrium), which have not yet been extensively modified by later hydrothermal maturation (Fig. 3).

Exploring this phenomenon in more detail, we find that pyrite samples from the anhydrite veins in the lower part of the TAG mound (Fig. 2c) have low δ^{56}Fe values that overlap the values of massive sulfide (Fig. 3, Table 1). Notably, the majority of these δ^{56}Fe$_{pyrite}$ values are lower than the δ^{56}Fe values of co-existing chalcopyrite from the veins. This confirms iron isotopic disequilibrium in this pyrite group, since pyrite should have higher δ^{56}Fe values than those of chalcopyrite if in isotopic equilibrium (Δ^{56}Fe$_{pyrite-chalcopyrite} \approx 0.9$‰ at 350 °C)[31]. The
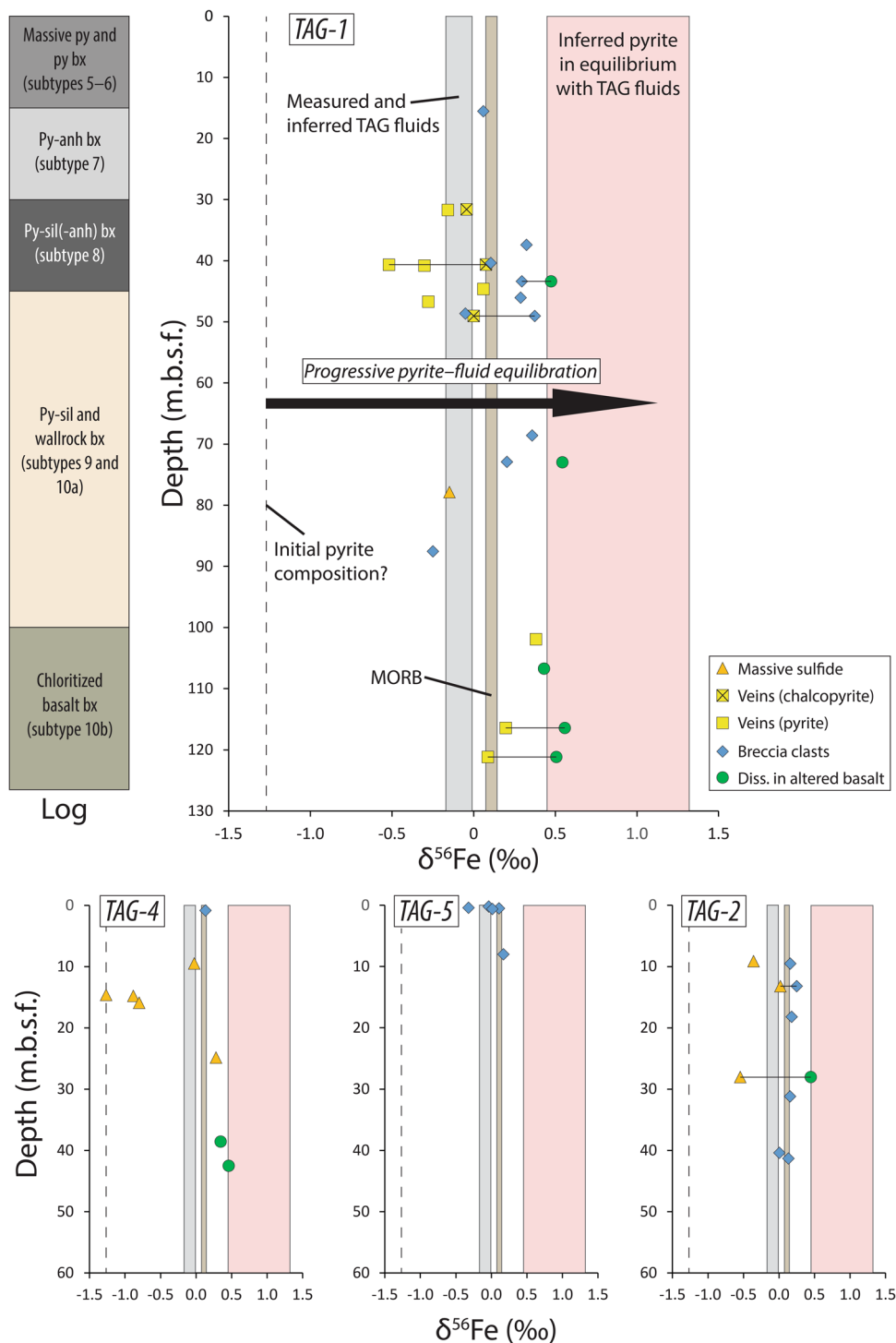
Fig. 3 Iron isotope results. The $\delta^{56}Fe$ values of pyrite ($n = 47$) and chalcopyrite ($n = 3$) from TAG-1, TAG-2, TAG-4, and TAG-5, respectively, are plotted as a function of depth below the mound surface. Tie-lines connect sulfide samples obtained from the same drill core piece. Included are the core log for TAG-1[44] and reference fields for MORB (brown)[23,56] and for measured[28] and inferred TAG hydrothermal fluids (gray). The inferred range of $\delta^{56}Fe$ values of pyrite in equilibrium with recent TAG hydrothermal fluids (pink) was calculated using the fractionation factors of ref. [30] and ref. [34]. The lowest $\delta^{56}Fe_{pyrite}$ value of our dataset ($-1.27‰$; TAG-4) is used to illustrate a potential initial (disequilibrium) iron isotope composition of pyrite formed via inferred iron (poly)sulfide precursors (dashed black line; cf. ref. [34]). We interpret the observed range of $\delta^{56}Fe$ values of different textural types of pyrite to reflect contrasting precipitation mechanisms (hydrothermal fluid–seawater mixing vs. conductive cooling) and variable degrees of progressive hydrothermal maturation during the evolution of the TAG complex. See text for details. anh anhydrite, bx breccia, diss. disseminated, py pyrite, sil silica.

presence of large volumes of associated anhydrite suggests that the pyrite formed recently ($\lesssim 100$ years ago[37], see above) due to mixing between hydrothermal fluid and entrained oxygenated seawater within the mound[59]. Similar to the massive sulfide, the

low $\delta^{56}Fe_{pyrite}$ values of the anhydrite veins can thus be explained by rapid pyrite precipitation followed by only very limited hydrothermal maturation and iron isotopic equilibration with later fluids (Fig. 3).

On the other hand, the coarser-grained pyrite from quartz-pyrite stringer veins in the TAG stockwork (Fig. 2e) have distinctly higher $\delta^{56}Fe$ values than those of pyrite from the anhydrite veins (Fig. 3, Table 1). At these deeper levels, i.e. below the anhydrite-rich zone of the mound, entrainment of seawater is decreased and pyrite precipitation is increasingly dominated by conductive cooling of the hydrothermal fluid[59]. As such, the rates of pyrite precipitation are slower and hence more substantial, albeit not complete, initial pyrite–fluid iron isotopic equilibration could occur during the formation of the quartz-pyrite stringer veins[26,34] (Fig. 3). Furthermore, crosscutting relationships confirm that these veins are older than the anhydrite veins[53] and have thus likely been subjected to more extensive hydrothermal maturation, leading to further increase in the $\delta^{56}Fe_{pyrite}$ values[30,34].

Pyrite in the sulfide clasts that occur in the different breccia types (Fig. 2d) show $\delta^{56}Fe$ values that are overall higher than, but in part overlap the $\delta^{56}Fe_{pyrite}$ values of the massive sulfide and the anhydrite veins. The values are similar to the $\delta^{56}Fe_{pyrite}$ values of the quartz-pyrite stringer veins, but are always lower than the estimated $\delta^{56}Fe$ values of pyrite in equilibrium with the TAG hydrothermal fluids (Fig. 3, Table 1). Pyrite in these clasts likely have diverse and possibly complex origins that involve combinations of mechanical and hydrothermal reworking of surficial (massive) and vein-related mineralization as well as in situ nucleation and growth of new pyrite[15]. Such heterogeneous pyrite assemblages should initially have $\delta^{56}Fe$ values similar to those of the massive and the vein-related pyrite described above, but the $\delta^{56}Fe_{pyrite}$ values will progressively shift to higher values as a result of variable degrees of hydrothermal maturation during the protracted development of the TAG breccias, thus offering a sensible explanation for the observed data spread in this particular sample group (Fig. 3).

Remarkably, the finely disseminated pyrite preserved within remnant fragments of altered basalt (Fig. 2e) has the highest $\delta^{56}Fe$ values observed at TAG, showing only minor overlap with $\delta^{56}Fe_{pyrite}$ values of the quartz-pyrite stringer veins and the sulfide breccia clasts (Fig. 3, Table 1). Within individual core samples, disseminated pyrite always has distinctly higher $\delta^{56}Fe$ values than those of pyrite that texturally overprints the altered basalt clasts (e.g., stringer veins or massive sulfide cement; Fig. 3). High-temperature hydrothermal alteration of the basaltic host rocks would have commenced during the initial stages of the evolution of TAG and involves chloritization followed by progressive paragonitization and silicification of the basalt, with pyrite forming throughout the alteration sequence[38,39]. Similar to the quartz-pyrite stringer veins, deeper hydrothermal conditions dominated by conductive cooling lead to slower rates of pyrite precipitation and increased initial pyrite–fluid iron isotopic equilibration. Clasts of variably altered basalt do not only occur in the TAG stockwork, however, but have also been incorporated into the mound breccias at depths much shallower than that expected for the top of the basement. The reason for this is poorly understood, but could potentially be related to high-velocity entrainment in hydrothermal fluid including hydrothermal explosions, or to processes akin to frost jacking and heaving during the repeated expansion (due to internal anhydrite precipitation) and collapse (anhydrite dissolution) of the TAG mound over several high-temperature hydrothermal cycles[15,38]. Disseminated pyrite preserved in the basalt clasts may thus represent the most extensively reworked sulfide sample material of this study. Such hydrothermal maturation appears to occur intermittently over tens of thousands of years during which the basaltic basement is progressively altered and incorporated into the TAG breccias[15,37–39], finally imparting a characteristic isotope signature of $\delta^{56}Fe_{pyrite}$ values in near-equilibrium to equilibrium with the hydrothermal fluids (Fig. 3). Complete iron isotopic equilibration during hydrothermal maturation is potentially aided by the finely disseminated nature of this pyrite, whereas such effects might be restricted to the surfaces of the more massive pyrite types described above.

In summary, we interpret the observed range of $\delta^{56}Fe$ values of different textural types of pyrite to reflect contrasting precipitation mechanisms (hydrothermal fluid–seawater mixing vs. conductive cooling) and variable degrees of progressive hydrothermal maturation during the evolution of the TAG mound and stockwork complex (Fig. 3). In contrast to the idealized rates suggested from experiments ($\gtrsim 1$ year to reach pyrite–fluid equilibrium[34]), our results suggest that iron isotopic equilibration of pyrite occurs over timescales of tens of thousands of years within large, dynamic and periodically inactive SMS deposits such as TAG, allowing the preservation of the $\delta^{56}Fe_{pyrite}$ variations that we observe. The observed iron isotope variations further imply that the W part of the TAG mound (TAG-4) has experienced less extensive hydrothermal maturation than the other parts, consistent with the mineralogical and geochemical asymmetry noted during the original ODP investigation[52]. Importantly, similar processes can probably explain iron isotope variations in sulfides from fossil onshore VMS deposits (e.g., immature, low-$\delta^{56}Fe$ 'black ores' and mature, high-$\delta^{56}Fe$ 'yellow ores'), such as the ones found in the classic Kuroko deposits of Japan[33]. Our study of TAG therefore concludes that sulfide iron isotope compositions can provide insight into the nature, longevity and dynamics of hydrothermal processes in SMS deposits and allow us to create a reference framework for future investigation of similar active and fossil hydrothermal systems elsewhere.

Methods

Sampling. Sub-seafloor samples from the TAG mound and stockwork were sourced from five drill cores (957C, 957E, 957H, 957M, and 957P) originally collected onboard R/V *JOIDES Resolution* during ODP Leg 158, September–November 1994[44] (Fig. 1b). Sulfide mineral separates, generally 10 to 100 mg, were extracted from cm-sized drill core pieces using a small-diameter electric drill. Petrographic examination aided the selection of monomineralic sampling sites; in a few cases, however, the fine intergrowths of sulfides only allowed for the recovery of mixtures (pyrite-chalcopyrite or pyrite-marcasite; Supplementary Data 1). The drill tip was repeatedly dipped into ethanol and cleaned using Kimwipes and compressed air between each sample extraction to avoid cross-contamination.

Iron isotope analysis. Iron isotope compositions of sulfide separate ($n = 50$) were determined at the Vegacenter at the Swedish Museum of Natural History in Stockholm. First, iron-bearing clays and silicates, variably present in separates from altered basalt ($n = 8$), were removed by dissolution in 10 M HF acid at room temperature for 3 days followed by centrifugation and rinsing of the residue with MilliQ-water. Complete removal of clays and silicates was then confirmed via powder X-ray diffraction (XRD) analysis using the instrumentation and protocol described in ref. [64]. The leached and unleached sulfide separates were then dissolved and purified for iron isotope analysis following a procedure adapted from ref. [65] and previously used in ref. [66]. About 15 mg of each sample was weighed and transferred to 7 ml Perfluoroalkoxy alkane vials. A volume of 1.5 ml 8 M HNO_3 was then added to each sample after which they were evaporated on a hotplate at 70 °C. Once dry, 0.75 ml concentrated HNO_3 and 0.5 ml 6 M HCl were added before evaporating the samples again. The evaporated residues were subsequently dissolved in 0.3 M HNO_3. For iron separation, aliquots of these solutions (each assumed to contain 200–300 µg Fe) were transferred to clean vials and diluted ten times with de-ionized water to obtain 0.03 M HNO_3. Purification was then done by anion exchange chromatography using 100–200 mesh AGMP-1M resin. After iron separation, the samples were dried and then converted to nitric form by repeated dissolution in concentrated HNO_3. The samples were finally dissolved in 5 ml 0.3 M HNO_3 prior to iron isotope analysis.

Iron isotope analysis was done using an Aridus II Nebulizer system coupled to a Nu Plasma II HR-MC-ICP-MS operated in medium-resolution mode (50 µm slit width, resolving power ~7000). This setup resulted in a sensitivity of ~6–9 V/ppm for $\delta^{56}Fe$ for solutions measured at 2 ppm Fe. The sample uptake rate was ~100 µL/min resulting in ~500 µL sample consumption per analysis. The instrumental iron background was 30–40 mV for $\delta^{56}Fe$ (~0.2–0.3% of sample intensity) based on on-mass zero measurements of pure 0.3 M HNO_3 at the beginning of each run. Each sample was measured six times in a row. The analyses were corrected for mass bias

by standard–sample bracketing using the IRMM-014 international standard. Results are reported as $\delta^{56}Fe$ and $\delta^{57}Fe$, which correspond to the deviations of $^{56}Fe/^{54}Fe$ and $^{57}Fe/^{54}Fe$ relative to IRMM-014 in per mil (Supplementary Data 1). The external reproducibility was 0.07‰ for $\delta^{56}Fe$ and 0.10‰ for $\delta^{57}Fe$ (2σ), based on repeated measurements of the Alfa Aesar standard solution[67] as an unknown throughout the analytical session. Data for samples and standards plot along a mass-dependent fractionation line in a $\delta^{56}Fe$ vs. $\delta^{57}Fe$ diagram (Supplementary Data 2), confirming that isobaric interferences were properly corrected for. Only $\delta^{56}Fe_{IRMM-014}$ values are discussed in the manuscript and figures and all cited literature data have been converted to the same scale.

Data availability

The authors declare that all relevant data are available within the article and its supplementary data files. The iron isotope data generated in this study have been deposited in the Figshare online open access repository accessible at https://doi.org/10.6084/m9.figshare.20134451.v1.

References

1. Corliss, J. B. et al. Submarine thermal springs on the Galapagos Rift. *Science* **203**, 1073–1083 (1979).
2. Rona, P. A. Hydrothermal mineralization at seafloor spreading centers. *Earth-Sci. Rev.* **20**, 1–104 (1984).
3. Hannington, M. D., de Ronde, C. E. J. & Petersen, S. In *Economic Geology One Hundredth Anniversary Volume* (eds. Hedenquist, J. W. et al.) 111–141 (Society of Economic Geologists, 2005).
4. Lusty, P. A. J. & Murton, B. J. Deep-ocean mineral deposits: metal resources and windows into earth processes. *Elements* **14**, 301–306 (2018).
5. Franklin, J. M., Gibson, H. L., Jonasson, I. R. & Galley, A. G. In *Economic Geology One Hundredth Anniversary Volume* (eds. Hedenquist, J. W. et al.) 523–560 (Society of Economic Geologists, 2005).
6. Martin, W., Baross, J., Kelley, D. & Russell, M. J. Hydrothermal vents and the origin of life. *Nat. Rev. Microbiol.* **6**, 805–814 (2008).
7. Dodd, M. S. et al. Evidence for early life in Earth's oldest hydrothermal vent precipitates. *Nature* **543**, 60–64 (2017).
8. Beard, B. L., Johnson, C. M., Von Damm, K. L. & Poulson, R. L. Iron isotope constraints on Fe cycling and mass balance in oxygenated Earth oceans. *Geology* **31**, 629–632 (2003).
9. Bennett, S. A. et al. The distribution and stabilisation of dissolved Fe in deep-sea hydrothermal plumes. *Earth Planet. Sci. Lett.* **270**, 157–167 (2008).
10. Tagliabue, A. et al. Hydrothermal contribution to the oceanic dissolved iron inventory. *Nat. Geosci.* **3**, 252–256 (2010).
11. Sander, S. G. & Koschinsky, A. Metal flux from hydrothermal vents increased by organic complexation. *Nat. Geosci.* **4**, 145–150 (2011).
12. Saito, M. A. et al. Slow-spreading submarine ridges in the South Atlantic as a significant oceanic iron source. *Nat. Geosci.* **6**, 775–779 (2013).
13. Conway, T. & John, S. Quantification of dissolved iron sources to the North Atlantic Ocean. *Nature* **511**, 212–215 (2014).
14. Hannington, M. D., Jonasson, I. R., Herzig, P. M. & Petersen, S. In *Seafloor Hydrothermal Systems: Physical, Chemical, Biological, and Geological Interactions, Geophys. Monogr. Ser. 91* (eds. Humphris, S. E. et al.) 115–157 (American Geophysical Union, 1995).
15. Knott, R., Fouquet, Y., Honnorez, J., Petersen, S. & Bohn, M. Petrology of hydrothermal mineralization: a vertical section through the TAG mound. in *Proc. ODP. Sci. Results* 158 (eds. Herzig, P. M. et al.) 5–26 (Ocean Drilling Program, 1998).
16. Doyle, M. G. & Allen, R. L. Subsea-floor replacement in volcanic-hosted massive sulfide deposits. *Ore Geol. Rev.* **23**, 183–222 (2003).
17. Piercey, S. J. A semipermeable interface model for the genesis of subseafloor replacement-type volcanogenic massive sulfide (VMS) deposits. *Econ. Geol.* **110**, 1655–1660 (2015).
18. Nozaki, T. et al. Subseafloor sulphide deposit formed by pumice replacement mineralisation. *Sci. Rep.* **11**, 8809 (2021).
19. Humphris, S. E. et al. The internal structure of an active sea-floor massive sulphide deposit. *Nature* **377**, 713–716 (1995).
20. Zierenberg, R. A. et al. The deep structure of a sea-floor hydrothermal deposit. *Nature* **392**, 485–488 (1998).
21. Barriga, F. J. A. S., Binns, R. A., Miller, D. J. & Herzig, P. M. (eds.). In *Proc. ODP. Sci. Results* 193 (Ocean Drilling Program, 2007).
22. de Ronde, C. E. J., Humphris, S. E., Höfig, T. W. & Reyes, A. G., the IODP Expedition 376 Scientists. Critical role of caldera collapse in the formation of

23. Johnson, C. M., Beard, B. L. & Weyer, S. *Iron Geochemistry: an Isotopic Perspective* (Springer, 2020).
24. Sharma, M., Polizzotto, M. & Anbar, A. Iron isotopes in hot springs along the Juan de Fuca Ridge. *Earth Planet. Sci. Lett.* **194**, 39–51 (2001).
25. Rouxel, O., Fouquet, Y. & Ludden, J. N. Subsurface processes at the Lucky Strike hydrothermal field, Mid-Atlantic Ridge: evidence from sulfur, selenium, and iron isotopes. *Geochim. Cosmochim. Acta* **68**, 2295–2311 (2004).
26. Rouxel, O., Shanks, W. C. III, Bach, W. & Edwards, K. J. Integrated Fe- and S-isotope study of seafloor hydrothermal vents at East Pacific Rise 9–10°N. *Chem. Geol.* **252**, 214–227 (2008).
27. Rouxel, O., Toner, B. M., Manganini, S. J. & German, C. R. Geochemistry and iron isotope systematics of hydrothermal plume fall-out at East Pacific Rise 9°50′N. *Chem. Geol.* **441**, 212–234 (2016).
28. Severmann, S. et al. The effect of plume processes on the Fe isotope composition of hydrothermally derived Fe in the deep ocean as inferred from the Rainbow vent site, Mid-Atlantic Ridge, 36°14′N. *Earth Planet. Sci. Lett.* **225**, 63–76 (2004).
29. Bennett, S. A. et al. Iron isotope fractionation in a buoyant hydrothermal plume, 5°S Mid-Atlantic Ridge. *Geochim. Cosmochim. Acta* **73**, 5619–5634 (2009).
30. Syverson, D. D., Borrok, D. M. & Seyfried, W. E. Jr Experimental determination of equilibrium Fe isotopic fractionation between pyrite and dissolved Fe under hydrothermal conditions. *Geochim. Cosmochim. Acta* **122**, 170–183 (2013).
31. Syverson, D. D. et al. Fe isotope fractionation between chalcopyrite and dissolved Fe during hydrothermal recrystallization: an experimental study at 350 °C and 500 bars. *Geochim. Cosmochim. Acta* **200**, 87–109 (2017).
32. Revels, B. N., Ohnemus, D. C., Lam, P. J., Conway, T. M. & John, S. G. The isotopic signature and distribution of particulate iron in the North Atlantic Ocean. *Deep Sea Res. Part II Top. Stud. Oceanogr* **116**, 321–331 (2015).
33. Otake, T. et al. Large Fe isotope fractionations in sulfide ores and ferruginous sedimentary rocks from the Kuroko volcanogenic massive sulfide deposits in the Hokuroku district, northeast Japan. *Geochim. Cosmochim. Acta* **295**, 49–64 (2021).
34. Pokrovski, G. S., Blanchard, M., Saunier, G. & Poitrasson, F. Mechanisms and rates of pyrite formation from hydrothermal fluid revealed by iron isotopes. *Geochim. Cosmochim. Acta* **304**, 281–304 (2021).
35. Lalou, C. et al. Geochronology of TAG and Snakepit hydrothermal fields, Mid-Atlantic Ridge: witness to a long and complex hydrothermal history. *Earth Planet. Sci. Lett.* **97**, 113–128 (1990).
36. Lalou, C. et al. New age data for Mid-Atlantic Ridge hydrothermal sites: TAG and Snakepit chronology revisited. *J. Geophys. Res. Solid Earth* **98**, 9705–9713 (1993).
37. Lalou, C., Reyss, J. L. & Brichet, E. Age of sub-bottom sulfide samples at the TAG active mound. in *Proc. ODP. Sci. Results 158* (eds. Herzig, P. M. et al.) 111–117 (Ocean Drilling Program, 1998).
38. Honnorez, J. J., Alt, J. C. & Humphris, S. E. Vivisection and autopsy of active and fossil hydrothermal alterations of basalt beneath and within the TAG hydrothermal mound. in *Proc. ODP. Sci. Results 158* (eds. Herzig, P. M. et al.) 231–254 (Ocean Drilling Program, 1998).
39. Petersen, S., Herzig, P. & Hannington, M. D. Third dimension of a presently forming VMS deposit: TAG hydrothermal mound, Mid-Atlantic Ridge, 26°N. *Miner. Depos.* **35**, 233–259 (2000).
40. Rona, P. A., Klinkhammer, G., Nelsen, T. A., Trefry, J. H. & Elderfield, H. Black smokers, massive sulphides and vent biota at the Mid-Atlantic Ridge. *Nature* **321**, 33–37 (1986).
41. Thompson, G., Mottl, M. J. & Rona, P. A. Morphology, mineralogy, and chemistry of hydrothermal deposits from the TAG area, 26°N Mid-Atlantic Ridge. *Chem. Geol.* **49**, 243–257 (1985).
42. Rona, P. A. et al. Active and relict sea-floor hydrothermal mineralization at the TAG hydrothermal field, Mid-Atlantic Ridge. *Econ. Geol.* **88**, 1989–2017 (1993).
43. Graber, S. et al. Structural control, evolution, and accumulation rates of massive sulfides in the TAG hydrothermal field. *Geochem. Geophys. Geosystems* **21**, e2020GC009185 (2020).
44. Humphris, S. E. et al. In *Proc. ODP. Init. Repts.* 158 (Ocean Drilling Program, 1996).
45. Herzig, P. M., Humphris, S. E., Miller, D. J. & Zierenberg, R. A. (eds.). In *Proc. ODP. Sci. Results* 158 (Ocean Drilling Program, 1998).
46. Humphris, S. E. & Kleinrock, M. C. Detailed morphology of the TAG active hydrothermal mound: insights into its formation and growth. *Geophys. Res. Lett.* **23**, 3443–3446 (1996).
47. Hannington, M. D., Galley, A. G., Herzig, P. M. & Petersen, S. Comparison of the TAG mound and stockwork complex with Cyprus-type massive sulfide

deposits. in *Proc. ODP. Sci. Results* 158 (eds. Herzig, P. M. et al.) 389–415 (Ocean Drilling Program, 1998).

48. Tivey, M. K., Humphris, S. E., Thompson, G., Hannington, M. D. & Rona, P. A. Deducing patterns of fluid flow and mixing within the TAG active hydrothermal mound using mineralogical and geochemical data. *J. Geophys. Res. Solid Earth* **100**, 12527–12555 (1995).

49. Edmond, J. M. et al. Time series studies of vent fluids from the TAG and MARK sites (1986, 1990) Mid-Atlantic Ridge: a new solution chemistry model and a mechanism for Cu/Zn zonation in massive sulphide orebodies. *Geol. Soc. Spec. Publ.* **87**, 77–86 (1995).

50. Edmonds, H. N. et al. Continuation of the hydrothermal fluid chemistry time series at TAG, and the effects of ODP drilling. *Geophys. Res. Lett.* **23**, 3487–3489 (1996).

51. Sohn, R. A. Stochastic analysis of exit fluid temperature records from the active TAG hydrothermal mound (Mid-Atlantic Ridge, 26°N): 1. Modes of variability and implications for subsurface flow. *J. Geophys. Res. Solid Earth* **112**, B07101 (2007).

52. Fouquet, Y., Henry, K., Knott, R. & Cambon, P. Geochemical section of the TAG hydrothermal mound. in *Proc. ODP. Sci. Results* 158 (eds. Herzig, P. M. et al.) 363–387 (Ocean Drilling Program, 1998).

53. Gemmell, J. B. & Sharpe, R. Detailed sulfur-isotope investigation of the TAG hydrothermal mound and stockwork zone, 26°N, Mid-Atlantic Ridge. in *Proc. ODP. Sci. Results* 158 (eds. Herzig, P. M. et al.) 71–84 (Ocean Drilling Program, 1998).

54. Rouxel, O., Dobbek, N., Ludden, J. & Fouquet, Y. Iron isotope fractionation during oceanic crust alteration. *Chem. Geol.* **202**, 155–182 (2003).

55. Chapman, J. B., Weiss, D. J., Shan, Y. & Lemburger, M. Iron isotope fractionation during leaching of granite and basalt by hydrochloric and oxalic acids. *Geochim. Cosmochim. Acta* **73**, 1312–1324 (2009).

56. Teng, F.-Z., Dauphas, N., Huang, S. & Marty, B. Iron isotopic systematics of oceanic basalts. *Geochim. Cosmochim. Acta* **107**, 12–26 (2013).

57. Janecky, D. R. & Shanks, W. C. Computational modeling of chemical and sulfur isotopic reaction processes in seafloor hydrothermal systems: chimneys, massive sulfides, and subjacent alteration zones. *Can. Mineral.* **26**, 805–826 (1988).

58. Blounot, C. W. & Dickson, F. W. The solubility of anhydrite ($CaSO_4$) in NaCl-H_2O from 100 to 450 °C and 1 to 1000 bars. *Geochim. Cosmochim. Acta* **33**, 227–245 (1969).

59. Brügmann, G. E., Birck, J. L., Herzig, P. M. & Hofmann, A. W. Os isotopic composition and Os and Re distribution in the active mound of the TAG hydrothermal system, Mid-Atlantic Ridge. in *Proc. ODP. Sci. Results* 158 (eds. Herzig, P. M. et al.) 91–100 (Ocean Drilling Program, 1998).

60. Zhu, X. K., O'Nions, R. K., Guo, Y. & Reynolds, B. C. Secular variation of iron isotopes in North Atlantic deep water. *Science* **287**, 2000–2002 (2000).

61. Butler, I. B., Archer, C., Vance, D., Oldroyd, A. & Rickard, D. Fe isotope fractionation on FeS formation in ambient aqueous solution. *Earth Planet. Sci. Lett.* **236**, 430–442 (2005).

62. Polyakov, V. B. & Soultanov, D. M. New data on equilibrium iron isotope fractionation among sulfides: constraints on mechanisms of sulfide formation in hydrothermal and igneous systems. *Geochim. Cosmochim. Acta* **75**, 1957–1974 (2011).

63. Velasco-Acebes, J. et al. Isotope geochemistry tracks the maturation of submarine massive sulfide mounds (Iberian Pyrite Belt). *Miner. Depos.* **54**, 913–934 (2019).

64. Sahlström, F. et al. Interaction between high-temperature magmatic fluids and limestone explains 'Bastnäs-type' REE deposits in central Sweden. *Sci. Rep.* **9**, 15203 (2019).

65. Craddock, P. R., Rouxel, O. J., Ball, L. A. & Bach, W. Sulfur isotope measurement of sulfate and sulfide by high-resolution MC-ICP-MS. *Chem. Geol.* **253**, 102–113 (2008).

66. Troll, V. R. et al. Global Fe–O isotope correlation reveals magmatic origin of Kiruna-type apatite-iron-oxide ores. *Nat. Commun.* **10**, 1712 (2019).

67. Fehr, M. A., Andersson, P. S., Hålenius, U. & Mörth, C.-M. Iron isotope variations in Holocene sediments of the Gotland Deep, Baltic Sea. *Geochim. Cosmochim. Acta* **72**, 807–826 (2008).

68. Ryan, W. B. F. et al. Global multi-resolution topography synthesis. *Geochem. Geophys. Geosystems* **10**, Q03014 (2009).

69. Grant, H. L. J., Hannington, M. D., Petersen, S., Frische, M. & Fuchs, S. H. Constraints on the behavior of trace elements in the actively-forming TAG deposit, Mid-Atlantic Ridge, based on LA-ICP-MS analyses of pyrite. *Chem. Geol.* **498**, 45–71 (2018).

70. Roman, C. & Singh, H. A self-consistent bathymetric mapping algorithm. *J. Field Robot.* **24**, 23–50 (2007).

71. Tivey, M. K., Mills, R. A. & Teagle, D. A. Temperature and salinity of fluid inclusions in anhydrite as indicators of seawater entrainment and heating in the TAG active mound. In *Proc. ODP. Sci. Results* 158 (eds. Herzig, P. M. et al.) 179–190 (Ocean Drilling Program, 1998).

Acknowledgements

Author contributions

F.S., S.S.P., and V.R.T. conceived the study. Micro-sampling was carried out by F.S. and iron isotope analysis was performed by E.K. at Vegacenter. Data interpretation and manuscript preparation was carried out by F.S. with contributions from V.R.T., S.S.P., X-Y.Z., and E.K.

Funding

Competing interests

The authors declare no competing interests.

Additional information

Supplementary information The online version contains supplementary material available at https://doi.org/10.1038/s43247-022-00518-2.

Correspondence and requests for materials should be addressed to Fredrik Sahlström.

Peer review information *Communications Earth & Environment* thanks Fernando Tornos and Drew Syverson for their contribution to the peer review of this work. Primary Handling Editors: Joe Aslin. Peer reviewer reports are available.

Reprints and permission information is available at http://www.nature.com/reprints

Publisher's note Springer Nature remains neutral with regard to jurisdictional claims in published maps and institutional affiliations.